Testing of a Prototype G^0 Detector Assembly

A thesis submitted in partial fulfillment of the requirement
for the degree of Bachelor of Science with Honors in
Physics from the College of William and Mary in Virginia,

by

Sandy Sligh

Accepted for _____
    (Honors, High Honors or Highest Honors)

_____
Advisor: Dr. David S. Armstrong

_____

_____

_____

_____

Williamsburg, Virginia
May 1999

Contents

List of Figures

iv

List of Tables

Abstract

The internal structure of the nucleon is not well understood from the fundamental perspective of Quantum Chromodynamics. The contribution of the strange quark to the makeup of the proton is parameterized in the G_E^0 and G_M^0 flavor-singlet charge form factors, yet these quantities have never directly been measured experimentally. The G^0 experiment, E91-017, at Thomas Jefferson National Accelerator Facility, plans to provide a clearer understanding of how the proton is structured internally. It will use parity-violating electron-nucleon scattering to ultimately yield an empirical value for the G_E^0 and G_M^0 form factors. This experiment will be a measurement in the range $0.1 \leq Q^2 \leq 1.0$ GeV^2, where $-Q^2$ is the 4-momentum transfer squared. Based on results from the SAMPLE experiment at the Bates laboratory, this experiment should be able to determine G^0 to about 3% accuracy. The experiment will be conducted in Hall C, using an azimuthally-symmetric, iron-free toroidal spectrometer, with a solid angle acceptance of 0.5 steradians.

Before major construction commences on the full G^0 detector, the testing of a single prototype detector element was crucial in flushing out design flaws and determining operational characteristics and efficiency. The full detector will be comprised of 256 individual scintillator-lightguide-PMT elements. Efficiency and resolution tests are required to determine if the current design for the G^0 apparatus is sufficient to ultimately measure $G_{E,M}^0$. The unconventional design of the detector elements and the challenges that this poses, dictated the need for the construction and testing of the prototype. This is the main focus of this thesis. It will examine the mechanical aspects of the prototype but more

importantly, the ability of the prototype to detect minimum-ionizing particles, the variation of light output over the detector, and the timing resolution. The results have shown that the prototype detector performance is well within design specifications.

Chapter 1

Introduction

1.1 TJNAF E91-017 Collaboration

TJNAF experiment E91-017 is a large experiment with many collaborators. Two engineering firms, four accelerator facilities, and sixteen universities are connected to the G^0 collaboration. The spokesman for G^0 is Douglas Beck from the University of Illinois - Urbana Champaign. The schools involved include CalTech, Carnegie Mellon, W&M, Hampton U., IPN Orsay, IPN Grenoble, Louisiana Tech, New Mexico State U., North Carolina A&T State U., U. of Connecticut, UIUC, University of Manitoba, UMD - College Park, U. of Massachusetts, University of Northern British Columbia, and Virginia Tech. The accelerator facilities include Fermilab, SLAC, TRIUMF, and TJNAF. The engineering firms are BWX Technologies and Bartozek Engineering. The official members of the G^0 collaboration at William and Mary are Dr. David Armstrong, Dr. Todd Averett, Dr. Michael Finn, Dr. Keith Griffioen, and Dr. Julie Roche. Two graduate students, Kevin Kramer and Dan Steiner and two undergraduate students, Jennifer Knowles and myself were actively involved

in the prototype construction and testing aspect of the experiment.

1.2   Acknowledgments and Contacts

I would like to thank the Department of Physics at the College of William and Mary for providing me with a superb physics education as well as the opportunity to work on such an engaging research project.

I would like to thank Dr. Todd Averett for helping me polish up my thesis during a difficult time for Dr. Armstrong. I also valued his advice to me concerning graduate school and invaluable assistance during the course of my research. I would also like to thank Julie Roche, the French Postdoc who was brave enough to work with me, a fast talking, hyperactive American, and also for helping me revise my thesis.

I would like to thank my fellow undergraduate physics majors at W&M, especially Dan Reid and TJ Walls, for numerous late night homework sessions and their support through the good, the bad, the hard, and the easy. I hope that sometime in the future, the three of us can return to William Small Memorial Hall, or perhaps Denny's, so we can reminisce about the great times we had over these past four years.

I would like to thank my family, my roommate Adam Aaronson, all the incredible guys from Spotswood Third Lower, and every one of the great friends that I made while at William and Mary. I thank them for putting up with my crazy hours and being polite whenever I start talking about physics.

Last, but definitely not the least, I would like to thank my advisor Professor David Armstrong who has provided extremely valuable support over the

entire course of this thesis. I would like to thank him for turning me on to Experimental Nuclear Physics, a field that I intend to pursue in Graduate School at UIUC. I will remember and value my experience working on this experiment with him forever. I was remember always the courage and strength displayed by Dr. Armstrong during a difficult time in his life. I was not sure whether to be grateful or angry when he returned to work so soon and amongst other obligations, helped me finish my thesis and prepare for my oral presentation. Dr. Armstrong is a great professor and a great man. I wish him all the best.

Contacts:

- Sandy Sligh

  email: sdslig@physics.wm.edu

  C.S. Unit 2752, 200 Richmond Road.

  Williamsburg, VA 23186-0753 (Valid until May 11, 1999)

  6515 Potomac Ave. Alexandria, VA 22307 (Permanent address)

  I will be attending the University of Illinois - Urbana Champaign

  Ph.D. program in physics beginning August, 1999.

- Professor David Armstrong

  email: armd@physics.wm.edu

  http://physics.wm.edu/~armd

  Department of Physics, The College of William and Mary

  Williamsburg, VA 23187

Chapter 2

Physics Relevant to G^0

2.1 Electromagnetic and Weak Probes of the Proton

Quantum Chromodynamics provides an accurate description of the interactions between valence quarks, the particles that make up a nucleon, and the gluons, the exchange particle of the strong nuclear force [1]. Quarks, when close together, are bound rather weakly. If an attempt is made to separate two quarks, the energy of the interactions between the quarks increases. In the environment of a nucleon such as a proton, the valence quarks (u-u-d) are separated by a relatively large distance. These interactions provide energy that along with the Heisenberg Uncertainty Principle allows for generation of quark-antiquark pairs. Thus, in addition to the three valence quarks, the proton is expected to contain a sea of quark-antiquark pairs.

This quark-antiquark pair production occurs on extremely short time scales, on the order of 10^{-20} seconds. Despite this fact, these pairs may have an effect upon the mass, spin, charge density, and magnetization of the proton. The

mass of the charm, bottom, and top quarks are rather large, and therefore appear too infrequently, to have a noticeable effect on the properties of the proton. Thus the creation of $u\bar{u}$, $d\bar{d}$, and $s\bar{s}$ pairs provide the most prominent contribution. Since up and down quarks are, according to both theory and experiment, are the primary components of the proton, obtaining clues to the contribution of the strange quark is a main goal of TJNAF experiment E91-017 [2].

When electrons and protons collide, there are two possible modes of interaction. The electromagnetic interaction will result in the exchange of a virtual photon between the two particles. This interaction is both charge dependent and helicity (spin polarization of the incident electron beam) independent. If one is interested in determining the strange quark contribution to the proton, charge dependence creates a problem because the electromagnetic interaction will couple to the d and s quarks with the same strength, due to both quarks having the same charge. A second way in which the electron and proton can interact is through the weak interaction. This will result in the exchange of either the Z^0 boson or the $W^\pm$ bosons. The $W^\pm$ weak interaction governs radioactive decay processes while the Z^0 interaction is exchanged in the same manner as a photon in the electromagnetic mode. The Z^0 interaction is charge independent and, most importantly, helicity dependent. The G^0 form factor is unique in that only through weak interaction (Z^0) with the proton does this form factor appear. This weak dependence is given explicitly as:

$$G_E^{P,Z} = \left(\frac{1}{2} - \sin^2\theta_W\right)G_E^{P,\gamma} - \frac{1}{4}G_E^{0,P} \qquad (2.1)$$

The definition of G_E^0 is shown in Eq. 2.2;

$$G_E^{0,P} = \frac{1}{3} \left(G_E^{u,p} + G_E^{d,p} + G_E^{s,p} \right) \tag{2.2}$$

where θ_W is the Weinberg mixing angle (a similar relation holds true for G_M^0). $G_E^{P,\gamma}$ is the electromagnetic form factor for the proton. The G_E^0 form factor in Eq. 2.2 (the electric case) contains the average of the up, down, and strange quark distributions within the proton. A feature of this G^0 form factor is that it may be extracted from asymmetry measurements using only proton form factors, i.e. no neutron form factors are needed. This feature is important because the neutron form factors are generally not known as accurately as the proton form factors.

The weak interaction will be stronger for negative helicity electrons than for positive helicity electrons. This gives rise to a non-zero scattering asymmetry with a dependence on the helicity of the electron beam, i.e. the probability of scattering is different for positive and negative helicity incident electrons. Therefore, an accurate determination of this asymmetry will provide a method by which to directly investigate the G^0 form factors. A problem arises in that the strength of the weak interaction is greatly overshadowed by the strength of the electromagnetic interaction. The total amplitude of an electron - proton interaction appears like:

$$M = M_\gamma + M_Z \tag{2.3}$$

where M_γ and M_Z are the electromagnetic and weak interaction amplitudes respectively. Because M_γ is many orders of magnitude larger than M_Z, M_Z is

6

hard to measure. Of course, in quantum mechanics probabilities, rather than amplitudes are measured. Probabilities are the squares of amplitudes. Now the equation appears differently, with the addition of a crucial cross term:

$$|M|^2 = |M_\gamma|^2 + |M_Z|^2 + 2Re[M_\gamma M_Z]$$

Without the presence of this cross term, the weak interaction probability, $|M_Z|^2$, would be too small to influence $|M|^2$. Because the cross term is not negligible, the measurement of M_Z and therefore ultimately a calculation of $G_{E,M}^0$ is possible.

2.2   Experimental Method

The basic idea behind the experiment is pleasantly uncomplicated. The total scattering probability for electrons incident on a liquid hydrogen target (protons) should be different for the two helicity configurations of the polarized electron beam. Accurately measuring this expected scattering asymmetry will allow for a precise measurement of M_Z and eventually $G_{E,M}^0$, given that the asymmetry, A, is directly proportional to M_Z[2][3],

$$A = \frac{|M^+|^2 - |M^-|^2}{|M^+|^2 + |M^-|^2} \propto \frac{2Re[M_Z M_\gamma]}{|M_\gamma|^2} \tag{2.4}$$

where M^+ are positive helicity interactions and M^- denotes a negative helicity interaction. To experimentally measure M_Z, the scattering probabilities in Eq. 2.4 are observed physically as numbers of scattered particles seen by

the detector.

$$A = \frac{N^+ - N^-}{N^+ + N^-} \qquad (2.5)$$

where N^+ and N^- are the number of scattered particles for positive and negative helicity configurations respectively. The asymmetry, A, might appear simple to obtain, however, A is on the order of 10^{-6} and is therefore challenging to measure. Because A is so minute, small variations in beam position, charge, energy or noise in the electronics that are helicity dependent can create false asymmetries. During the data taking period it will be important to monitor the beam characteristics carefully in order to prevent false asymmetries from influencing the results. To further minimize these false asymmetries, it is important that the response of each detector element not vary for particles hitting the detector at different locations. The location of particles intersecting the detector is correlated to where the electron beam hits the target and beam position can vary for different helicity configurations. Thus, one goal of the present measurement was to examine the variation in the prototype detector's response over it's area.

Chapter 3

Prototype Construction

3.1 Overview of Focal-Plane Detector Design

The full focal-plane detector will consist of 8 octants, arranged symmetrically around the beamline axis. Each octant will consist of 16 pairs of arc shaped plastic scintillators, as seen in Fig. 3.1. Each scintillator will have two acrylic lightguides attached at each end, and coupled to the end of each light guide will be a Philips XP2262, 12 stage Photomultiplier tube. These particular scintillator shapes are dictated by the physics of the spectrometer. Each particle scattered from the target follows a path determined by its momentum transfer and the presence of an approximately 1T toroidal magnetic field. The predicted paths of the scattered particles in the magnetic field created by the superconducting magnets are shown in Fig. 3.2. Scattered particles with a high momentum will be bent less by the magnetic field and will intersect the scintillators which are lower on the octant. The opposite is true for particles with a low momentum. Each detector is designed to measure a fixed range of Q^2 along its entire length.
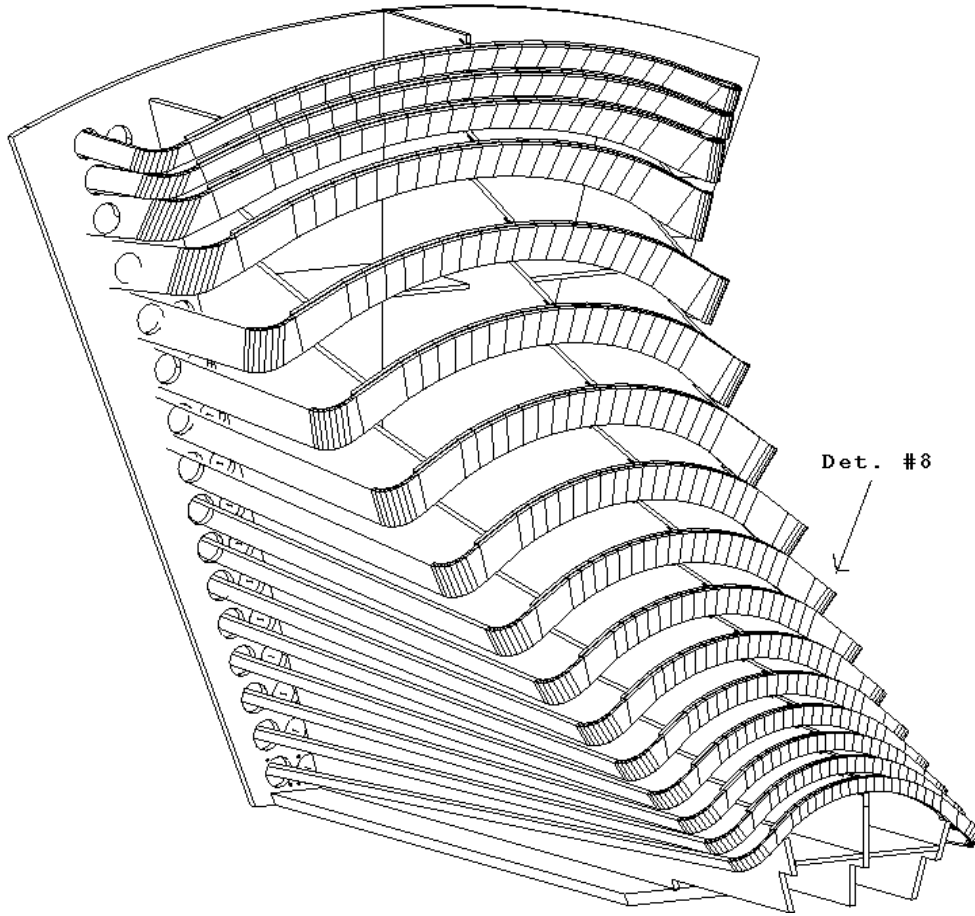
Figure 3.1: Single octant of G^0 detector assembly.

The lack of space between adjacent detector octants prevents the PMTs from being placed in conventional locations, at the end of each scintillator arc. In addition, the presence of a strong magnetic field in the area of the scintillators provides another design challenge. A photomultiplier tube's operation includes the acceleration of photoelectrons. The presence of a strong magnetic field would prevent photoelectrons from being accelerated from dynode to dynode, rendering the tubes ineffective. This property of PMTs prompted

10
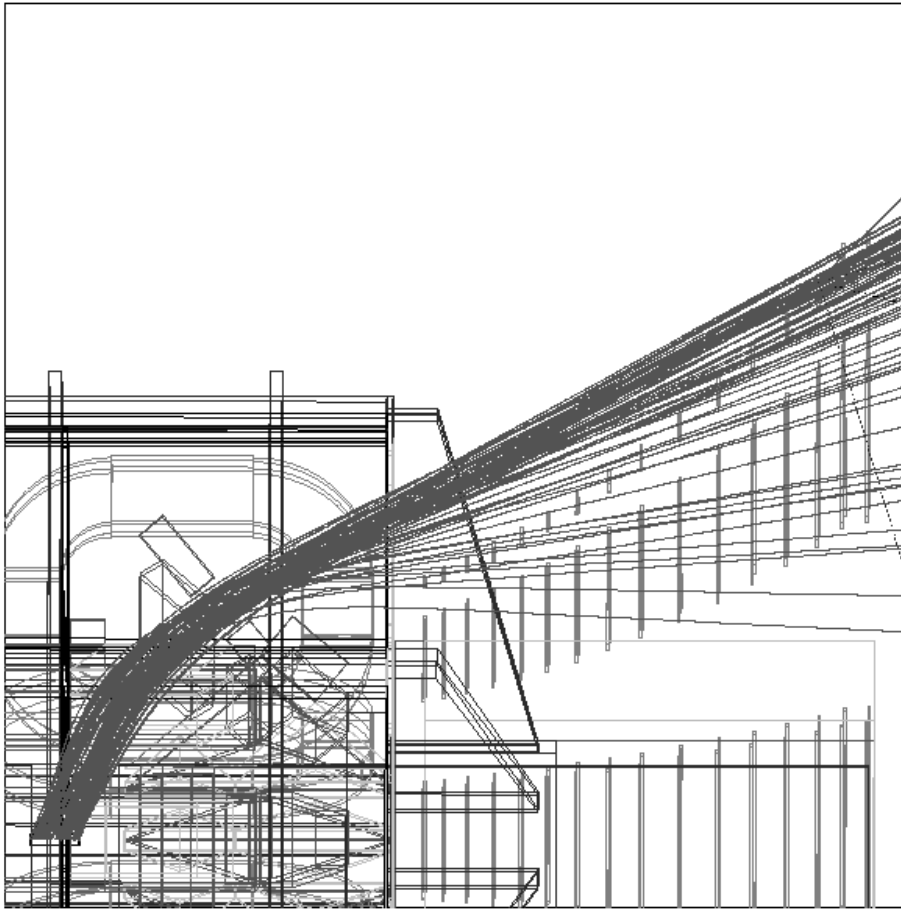
Figure 3.2: Side view of G^0 Detector, showing paths of scattered particles. The superconducting magnet and H_2 target (the area where the track lines are emanating) are shown on the left. A side view of the "Focal Plane" detector is shown on the right (the vertical lines are the scintillator arcs).

the design and construction of complicated light guides to allow the tubes to be located beyond the magnetic field. To examine the performance of the detector design, our group at William and Mary was provided a prototype of detector #8. Detector #8 is located midway up a detector octant. The complicated geometry of the light guides and the unsuccessful initial attempts to

mate the prototype's light guides to the scintillators during the assembly of the
#8 prototype, illustrates the usefulness of constructing a prototype. Between
AutoCAD models, two dimensional schematics and actual physical fabrication
of the light guides and support assembly, design and fabrication errors were
discovered. This forced the W&M members of the G^0 collaboration to take
time aside from testing the prototype to determine the precise origin of the
problems.

During the summer of 1998, the members of the William and Mary G^0
collaboration received the components of the detector #8 prototype. This
consisted of the large aluminum support structure. This structure is designed
with three support ribs (in the ultimate construction of the full G^0 detector
octants, it has been decided to remove the middle rib). These ribs hold the
scintillators in place, and the light guides are attached to the side of the two
outer ribs. A photograph of the prototype is shown in Fig. 3.3 and depicts the
ribs and where the light guides mate to the outer ribs. The arc-shaped pieces
(it's difficult to see that there are two, as they are mounted back-to-back)
in the foreground are the scintillators, shown wrapped in aluminized mylar.
The scintillator arcs are 72 cm from end to end, 1 cm thick and 5.5 cm wide.
The prototype lightguides, which are 90 cm in length, are connected to the
scintillators and extend out the back of the prototype support assembly.

A digital photograph of where the lightguides exit the rear of the proto-
type is shown in Fig. 3.4. These exposed ends are then connected to the
photomultiplier tubes via a silicone cookie.

Figure 3.3: View of Detector #8 Prototype in a darkroom at William and Mary.

3.2   Construction of Prototype

Before testing, the prototype had to be assembled. This included wrapping and mounting the scintillators on their support ribs. The two arcs are wrapped in aluminized mylar to prevent contaminants (finger oils, among others) from crazing the plastic. Crazing is the formation of minute cracks or scratches
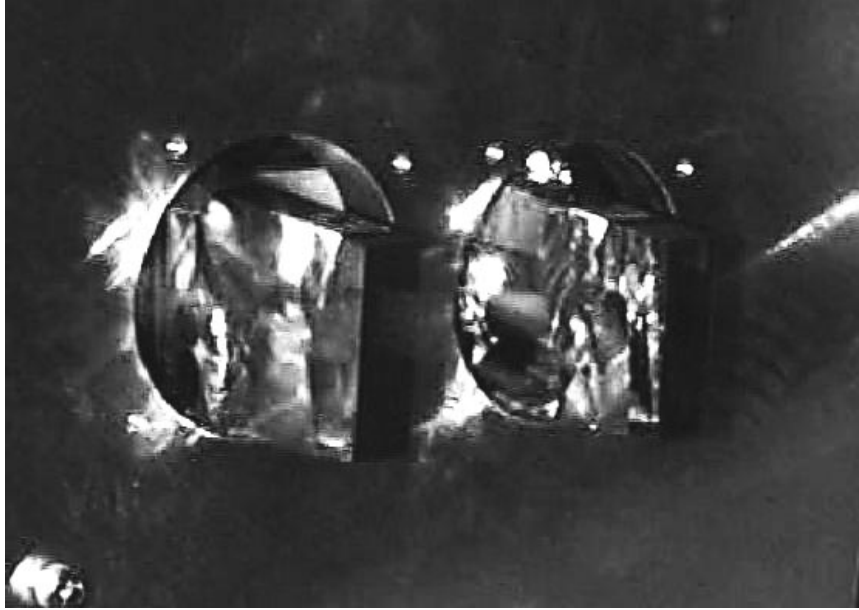
Figure 3.4: View of Left Lightguides Exiting the Prototype

throughout the plastic. Without a clean, smooth, and uniform surface, light bouncing around inside the plastic will hit the rough, crazed surface and will propagate erratically, increasing the probability of the light refracting out of the plastic. The wrapped arcs are held in place with 6 precision clips. Two clips on the top and bottom of the arcs are secured to each support rib. Once it was determined that the arcs would fit in their clips, the light guides had to be placed in their clamps to see if the guides and the arcs would mate flush, allowing the two to be affixed to each other via special adhesive. Unfortunately, somewhere along in the construction of the lightguides and/or the support apparatus, some design specification was misread or a fabrication method failed to bend the light guides properly. The lightguides in their clamps did not mate

14

flush with the scintillators. This discovery prompted a long investigation by the collaborators at W&M to determine the cause(s) of the design flaw.

Eventually, the causes were discovered. The angled support ribs were slightly off of alignment. This prevented the lightguides from coming into contact with the arcs. It was also noticed that the lightguides exhibited several millimeters of relaxation. It was inferred that when the lightguides were bent at Carnegie Mellon Univ., the jig that was used to hold the lightguides had different clamp locations from where the prototype was designed to be clamped. When the lightguides were installed, they seemed to pull away from the arcs, as if they were sagging. To solve the problem of the guides and the arcs not mating flush, a few adjustments were needed. The standoffs that held the guides away from the support ribs were machined down to allow the guides to approach close to the arcs. The clamps themselves were supplemented with rubber shims to allow finer adjustments. This ultimately worked well enough to allow the guides to be glued to the arcs. For the gluing, Dymax model #3069 UV-activated epoxy was used. This special epoxy is in liquid form; when irradiated with a UV Source Inc. "Emerald" UV lamp, the epoxy cures within 20 seconds. With the guides and arcs in place, the PMTs were attached to the rear of the prototype. The whole apparatus was placed inside a darkroom in the W&M physics building, as shown in Fig. 3.3.

Finally, to process the electronic information from the phototubes, an electronics chain was constructed by the members of the W&M G^0 collaboration. Each PMT signal arrives at the Data AcQuisition system, or DAQ, and is sent through a variety of logic modules. Eventually each tube supplies a signal

to an ADC, or Analog-to-Digital Converter, a Time-to-Digital-Converter, and the Coincidence Unit. For explanations of the operation of an ADC and a TDC, plus a schematic of the electronics chain, see the appendix.

Chapter 4

Prototype Testing

The main goal of the detector assembly will be to accurately and reliably count the electrons or protons scattered from the liquid H_2 target. Because of the unconventional shape of the scintillator pieces, the ability to resolve incident particles is not as well understood as with simple rectangular scintillator paddles. The fear is that the shape of the arcs will cause the photons to travel a longer path that they would in a rectangular scintillator. The light is attenuated as it travels down the scintillator, so a longer path might increase the chances that some of the meaningful events will be attenuated to undetectable levels. Simulation can give a rough understanding of the light propagation within the scintillator arcs, however direct testing of a prototype will give a more reliable impression. This is because in a simulation, quantities such as the reflectivity, attenuation per unit length, and other physical properties are usually assumed to be uniform throughout the material. Therefore, simulations do not have to consider variations in polish quality or crazing of the scintillator surface. Due to the possibility that such flaws may be present in the final detector assembly, physical prototyping is necessary. In spite of the

obvious higher cost of constructing a physical prototype as opposed to a simulation, physical testing is worthwhile and should yield meaningful results that can be compared and contrasted to simulation.

4.1   PMT Characteristics

With the exception of the actual scintillator plastic, the most important components of the G^0 Focal Plane Detector are the Photo Multiplier Tubes (PMTs). The PMTs will convert the photons created during the ionization in the plastic into an electronic signal which can be processed by the data acquisition electronics.

4.1.1   PMT Settling Time

During early testing of the detectors with a ^{106}Ru β source, it was noticed that the gain of the PMT's changed during the initial 10-20 minutes after the PMT were powered on. All previous data taken during this warmup period was rendered useless, as the rate of change within the tubes was unknown and possibly differed between tubes. To guarantee that any subsequent testing was done without having to worry about erratic tube behavior, specific tests were undertaken to determine a proper settling time for the tubes.

A ^{106}Ru β source was attached to the flat edge of the front scintillator and the presence of a signal in either of the back PMTs was the condition used to trigger the DAQ. The outputs for all four PMTs were captured by an ADC, or Analog-to-Digital Converter, for a total of 16 minutes and the results were histogrammed. An ADC measures pulse height which is proportional to the

amount of light collected by the PMT. A total of eight histograms were created, each histogram containing two minutes worth of ADC data. Each of these two minute histograms immediately follow one another, thus the eight histograms charted the change in ADC level over a period of sixteen minutes. The time-dependent behavior of all four tubes (the four G^0 PMTs will be referred to as FL, FR, BL, and BR for front left, front right, back left, and back right respectively) is shown in Fig. 4.1. The other three tubes were normalized to the FL tube. Because this will be a rough calculation, the normalization process is acceptable. From the data, it is obvious that the rate of change of the tubes gain is decreasing over time. To determine at what time this trend stabilizes efficiently, the various data points were compared to the asymptotic value given by the exponential function,

$$Y = A \exp\left(-t/\tau\right) + C$$

The values on the y-axis of Fig. 4.2 indicate the fractional error in the ADC centroid. This mean that, for example, at 15 minutes, the centroid value of the ADC peak is within 1% of the asymptotic value. After examining these results, it was decided that before any data can be collected from the PMT's, they must have at least fifteen minutes of "warm-up" time to guarantee that the tubes will not be a significant source of systematic error. Unfortunately, this decision slows down overall data collection considerably, especially during source testing which required frequent powering down of the tubes to physically move the source from one location to another.
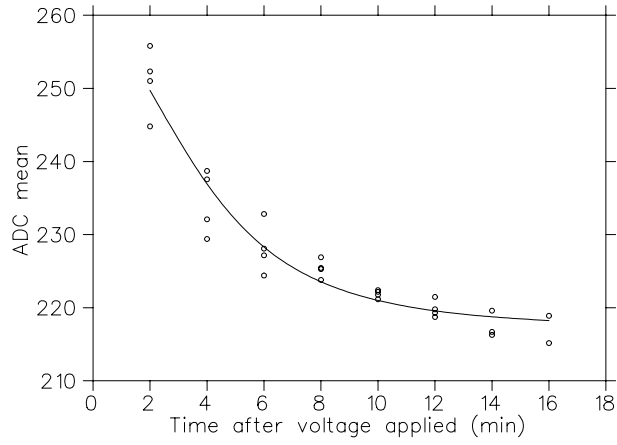
Figure 4.1: ADC centroid mean versus time. The results of the PMT settling time study is shown with an exponential function fit to the scaled data.
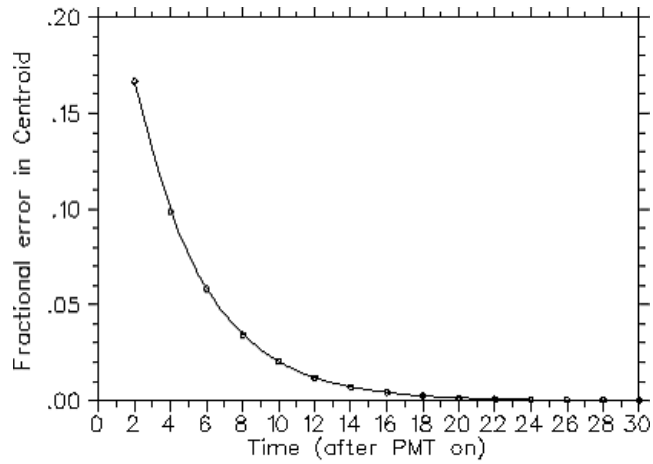

Figure 4.2: Fractional error in the centroid of the FL versus time. the fit's values are irrelevant because the interesting information from this fit is that after 15 minutes, the tubes are within 1% of the asymptotic value.

4.1.2 Single Photoelectron Detection

Each of the prototype's four PMTs are the Philips XP2262. Despite being the same model, each tube is unique in that even if all four PMTs are supplied with the same High Voltage (HV), and are hit with the same number of photons, their outputs will vary. Therefore, there needs to be a absolute way to calibrate the outputs of each PMT so that each PMT can be compared to one another.

There is a simple way to this. Consider two sets of concurrent data points, one for the FR tube and one for the FL. Find the ratio of the right set's mean to the left set's, then scale all the points in the right set (or left depending on which set you pick as "correct") by this ratio. This is how the data in section 4.2.1 were treated. This is an extremely dangerous method for, in averaging the data in this way, any information about how much light is actually reaching each tube is destroyed. This method was used during the source scans as a preliminary way to compare the shapes of the two graphs, and in so doing both left and right tubes are essentially set equal, when in fact they are not.

The output from a particular PMT is digitized by the ADC module and converted in arbitrary units of "channels". When light from the scintillator impacts the photocathode of the PMT, a discrete number of photoelectrons (p.e's) is ejected from the photocathode through the photoelectric effect. Therefore, the quantity subsequently stored in the ADC histogram should also correspond to the same number of photoelectrons. To determine exactly how many photoelectrons an "X" channel ADC signal corresponds to, the number of ADC channels that corresponds to a single photoelectron needs to be deter-

mined. Once ADC information for each PMT is calibrated to photoelectrons, the direct and absolute comparison of one tube to another is possible.

There are two quantities that need to be collected for each tube, the pedestal and the single photoelectron peak, which we amplify by a factor of 100 because the signals are very small and would be swallowed by noise from the radio station if the signal was not amplified. The pedestal is background noise that can be caused by thermionic emission of electrons within the PMT, electronic noise in the ADC module, a DC level in the electronics and also by the nearby WCWM radio transmitter. The pedestal is essentially a baseline for the electronics, the minimum signal that can be seen by the electronics. The pedestal information is collected by reducing the discriminator threshold to a minimum and letting the DAQ record whatever signals the PMTs produce. Figure 4.3 shows a typical pedestal peak.
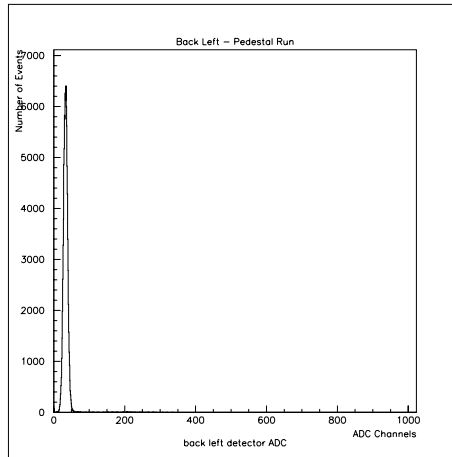

Figure 4.3: Number of events versus ADC channels. Example of a pedestal histogram for G^0 PMTs.

To collect the single photoelectron peak for each tube, a pulsed LED was used. The DAQ used a pulse generator as its trigger, and the same generator sent small pulses to the LED, on the order of a volt. The light produced by the LED is much to weak for human eyes but is detectable by the PMTs. Each miniscule pulse of light from the LED sends out many photons, however, the number of photons impacting the PMTs is not constant because the PMTs only detect a certain percentage of the incident photons.

> "..the number of photons hitting the photocathode is not a constant but rather a Poisson distributed variable. This (spectrum) follows from the fact that only a fraction of the incident photons is picked up by the PMT. The conversion of photons into electrons and their subsequent collection by the dynode system is a random binary process. Therefore the distribution of the number of photoelectrons can be expressed as a convolution of Poisson and binary processes. – Bellamy [5]"

Figure 4.4A depicts a single photoelectron peak around channel 225. When the power of the LED is sufficiently great, the histogram begins to change shape. The reason for the change is that the power of the LED has become great enough that the PMT is starting to measure occurances of 2 and more photoelectrons. If the power is increased further, the 3 and 4 photoelectron peaks start to dominate the distribution. How the ADC peak changes as the power of the LED is increased is shown in Fig. 4.4.

The presence of multiple p.e. peaks is not obvious since their peaks are

convoluted with a larger single p.e. distribution. To fit this compound function, a convolution of Gaussian and Poisson distributions is used, following the method outlined in Bellamy [5]. The value of the single photoelectron will be the centroid of the first Poisson curve in the fit. The fitting of the complicated spectrum in also shown in Fig. 4.4.
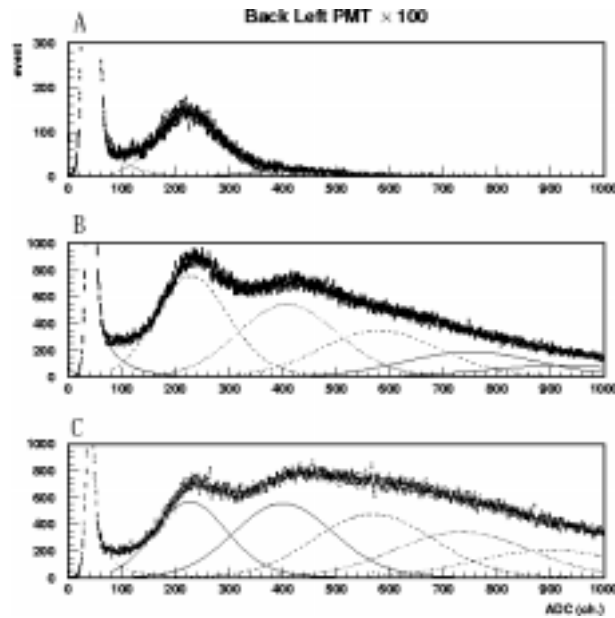
Figure 4.4: BL ADC spectra for different LED voltages. The smooth curves are fits to multiple Poisson curves.

When the single photon peak was isolated (Fig. 4.4A) a single Gaussian fit yielded centroid values only a few channels off from the results of the more complicated fit. On the whole, this technique of fitting multiple p.e. spectra is more precise than simply fitting a single Gaussian to Fig 4.4A, but in the end it just corroborates the results of the simpler fit. Subtracting the pedestal

from the single p.e. peak and dividing by 100 will give the number of channels per photoelectron for that particular PMT. Table 4.1 displays the "channels per p.e." values for the G^0 tubes.

PMT	HV	gain(channels/p.e.)
FL	2080V	1.77
FR	1875V	1.47
BL	2060V	1.82
BR	2000V	1.94

Table 4.1: Gains for the G^0 PMTs, as determined using the single photoelectron signals. The HV values are shown because changing the HV will change the gains for that tube.

With the values in Table 4.1, the four G^0 PMTs can be compared on an absolute scale, which will allow checks of how effective the G^0 detector design is in transmitting scintillation photons from the scintillator, down the lightguide, and to the PMTs.

4.2 Prototype Detector Response Testing

4.2.1 ^{106}Ru Source Scans

Source Scan Methodology

To determine how effective the G^0 prototype is in transmitting scintillation photons from the scintillators to the PMTs, an intensive study of both the front and back scintillator arcs was conducted using a ^{106}Ru source. ^{106}Ru is a radioactive isotope which, after a preliminary low-energy β decay, emits β particles with an endpoint energy of 3.5 MeV. The ^{106}Ru was collimated to define both the radial position and longitudinal (ϕ) position of the source and to better approximate the path of scattered electrons in the actual experiment. For a visual depiction of the scintillator arc and the parameters varied during the source scans, see Fig. 4.5.

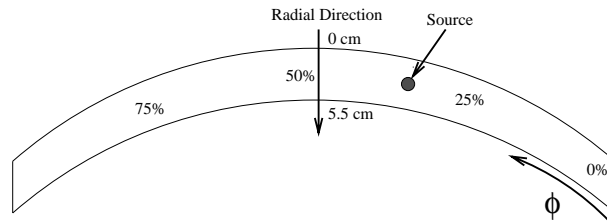Figure 4.5: A schematic representation of a scintillator arc, explaining "longitudinal" (ϕ), "radial",and "position" (the %'s).

Longitudinal Source Scans

The initial set of source scans were started at the left extreme of the prototype, near where the scintillator and the lightguides are mated. It is at these locations, both the left and right extremes, that two precision clips are located,

26

which hold both the front and back detectors in place. These locations were used as the starting and ending point of a full source scan. The area of scintillator between the two precision clips, about 60 cm, was divided into 6 cm segments. At each division, the source was placed at the radial midpoint of the scintillator arc (by using a micrometer) to ensure that only the ϕ position is being varied. While looking at the front ADC, the back arc was used as a trigger by putting the BL and BR discriminator outputs into an OR gate and using this output as the DAQ's trigger. This was done to ensure that only events that traversed the entire thickness of the front arc were recorded. The number of events per location was kept at a constant value also in order to ensure that the difference in the ϕ position of the source was the only variable. Once data had been collected at each of the 6 cm. divisions, these histograms were each fit to a Gaussian, and the centroids for the front (or back) right and left were plotted against each other. The centroids of one set were scaled to the other to make this comparison more meaningful. These data were collected before the PMT gains in Table 4.1 were determined. The reason for displaying these preliminary plots is to compare them to plots of the same data, calibrated with the values in Table 4.1, shown later.

The relationship between FL and FR without taking into consideration the radial position of the source, the PMT's settling time, or obtaining the same statistics at each position is shown in Fig. 4.6A. When these variables were controlled, the source scan results smooth out and look like Fig 4.6B. Besides the fact that the relationship between ADC centroid and ϕ position appears to be nearly linear, this test has shown that energetic particles interacting
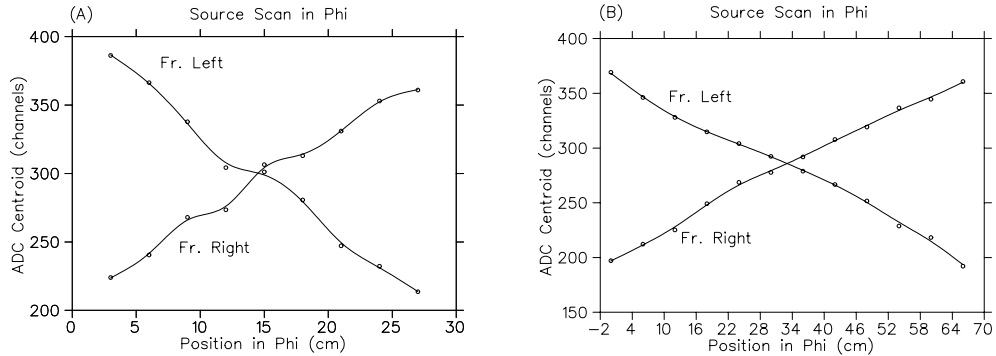
27

Figure 4.6: A) ADC centroid versus Phi position for the front detector with poor radial precision and without proper PMT settling. B) ADC Centroid versus Phi position with good radial precision and proper PMT settling

anywhere longitudinally along the scintillator will produce ADC values well above the 15 mV (approximately 9 channels) threshold of the electronics. This is encouraging result and will make a difference when the overall efficiency of the detector is tested later on.

To show how the phototubes actually compare to one another, the raw data from Fig. 4.6A was scaled using the calibration from Table 4.1. Figures 4.7A and 4.7B are front and back source scans scaled using the single p.e. calibrations. Note the significant difference between Fig. 4.6B and Fig. 4.7A. It appears that for an equivalent location on the detector the FR tube is getting more light that the FL tube. This could be due to a variety of reasons. The silicone cookie connecting the PMT to the lightguide could be pulling away, forming a new interface for the photons to refract through. The surface of the scintillator on the left side could be scratched or crazed. The glue joints between the lightguide and the scintillator could be of a poorer quality than the joint on the right side. Any one or any combination of these factors could

28

be contributing to the apparent loss of light in the left tube compared to the right tube. Cosmic ray scans, described in a later section will provide a another arena in which to compare tubes. On the other hand, the BR and BL tubes seem to be receiving the same amount of light, according to Fig. 4.7B. Note that the 15 mV threshold corresponds to approximately 5 photoelectrons.
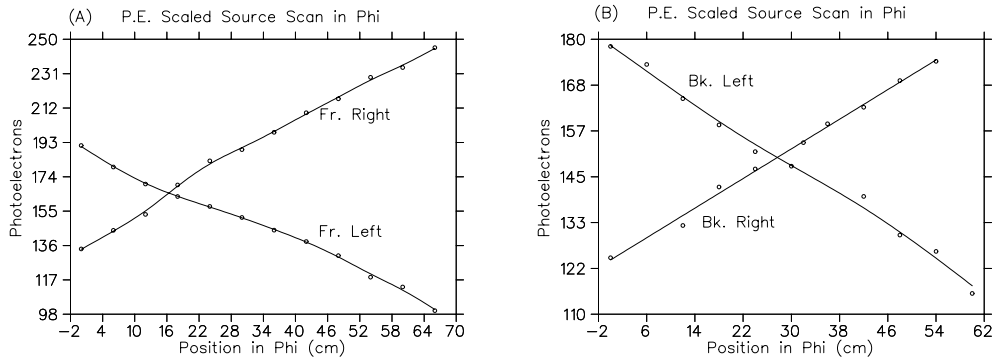

Figure 4.7: A) Photoelectrons versus position in ϕ; Front PMTs. B) Photoelectrons versus position in ϕ; Back PMTs

Radial [106] Ru Source Scans

The ADC response to variations in ϕ were examined in the previous section. It was mentioned that the reason for the improvement between the Fig. 4.6 A and B was due to three factors, one of which was paying close attention to the radial position of the [106]Ru source. The unconventional shape of the scintillator arcs might cause some of the photons created by the minimum ionizing electron to be attenuated down to undetectable levels. To examine this behavior, the 6 cm face of the arc, between the two clips, was divided into seven locations. The source was secured to the scintillator's face at these locations, and a run of 90,000 events was taken, similar to the runs taken

for the ϕ source scans. Each set of 7 radial positions were tested at three ϕ positions; 0% (the left extreme), 25%, and 50%. (for clarification, an extreme is where the scintillator is held by a precision clip and is very close to the scintillator/light guide interface). Runs were also taken at 75% but this was merely to check that the scintillator was symmetric, i.e. 25% and 75% should look the same. The radial scan at 0%, shown in Fig. 4.8, shows interesting behavior of the scintillated light incident upon the FL tube. The shape of FR's graph has a shape similar to the ϕ scans, although there appears to be an "S-like" shape. A geometric argument might offer an explanation of the shape.
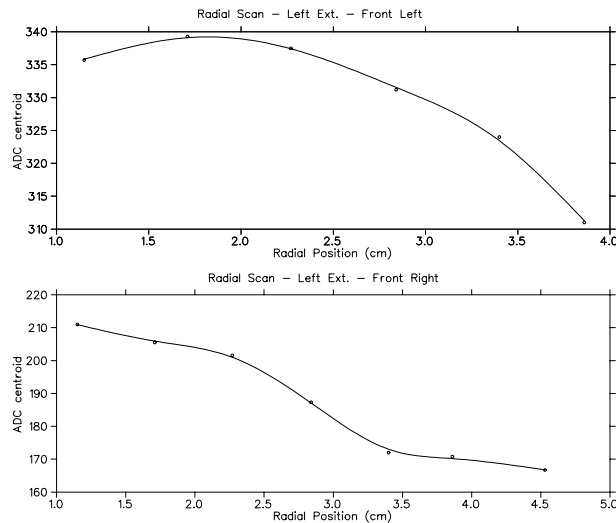

Figure 4.8: ADC centroid versus radial position (cm) at the left extreme (0%)

Figure 4.9 shows a possible explanation for the "S" shape of the right tube's ADC signal in Fig. 4.8. Positions 1 and 2 in Fig. 4.9 obviously have the biggest signals due to their similar short path lengths. Positions 3 and 4
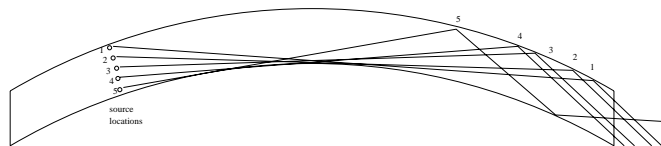
Figure 4.9: Geometric depiction of FR tube signal from Fig. 4.8

may account for the plateau region of the "S" curve since it appears that 3 and 4 have similar path lengths. Position 5 accounts for the low point of the "S" curve due to the many bounces of the light. The more bounces the light has to make in order to reach the PMTs, the higher the chance for the light to refract out of the detector. This figure is not entirely realistic since all the paths depicted attempt to go through a similar point. In reality, each source location has a myriad of possible paths and Fig. 4.9 shows only the shortest paths.

Having moved the source 15.3 cm away from the left extreme in Fig. 4.10 seems to have suppressed FL's "hump" shape visible in the top plot in Fig. 4.8. The "S" shape is still present for FR.

Finally, placing the source in the middle of the scintillator arc should produce right and left graphs that look virtually identical; this expected behavior is shown in Fig. 4.11. While the shapes of the graphs are interesting, they are not the most important features. As in the longitudinal scans, the fact that all the ADC signals registered above the electronics' threshold of 15 mV is good news. Due to the unconventional shape of the scintillator arcs, the ability to resolve incident electrons is of utmost importance. Both the radial
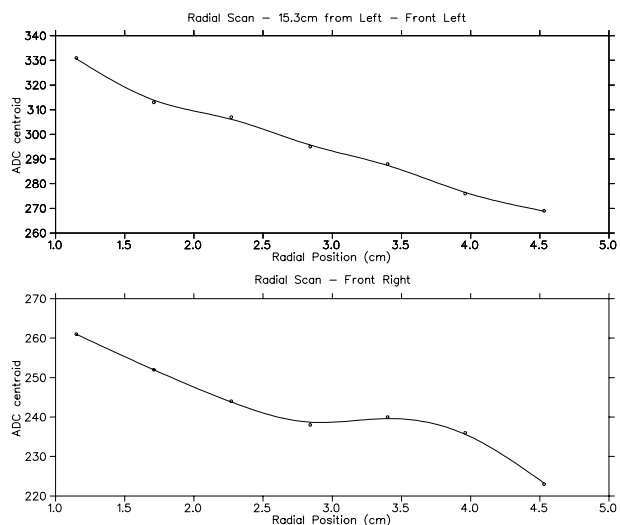
Figure 4.10: ADC centroid versus radial position at 25%. FL's shape has flattened out, while FR still exhibits "S" shape.
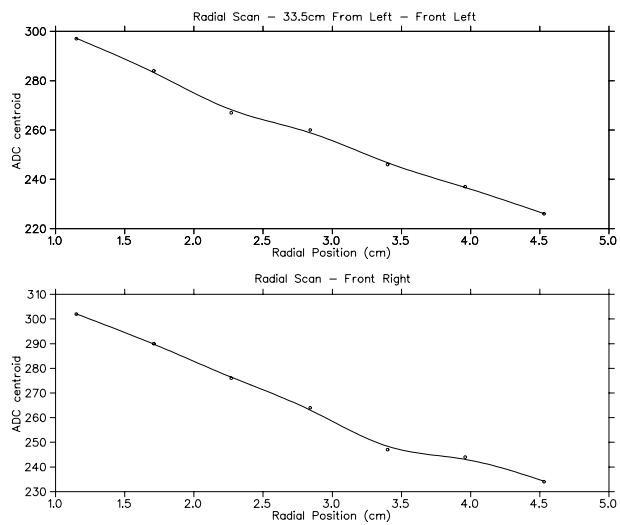

Figure 4.11: ADC centroid versus radial position at 50%. Both FL and FR have flattened out.

scans and the ϕ scans have shown that no matter where the electrons traverse the scintillator, the electronics will detect it. Variation in the longitudinal direction did amount to a factor of two, but it can be said with confidence that despite this variation, the pulse heights will always come into the electronics over threshold. In the radial case, at every location the fractional variation in pulse height was $\leq 15\%$.

4.2.2 Cosmic Ray Studies

When the experiment, E91-017, is ready to take real data, the energy of the particles that the detectors will be dealing with will be much larger than those emitted by the ^{106}Ru source. To test the prototype's ability to detect and resolve real physics events, cosmic rays can substitute for the scattered electron beam that will be used in the actual experiment. Even though the cosmic ray particles, (typically) muons, are of higher energy than the electrons at TJNAF, both the cosmic muons and the accelerator's electrons are minimum ionizing particles [4]. A minimum ionizing particle will deposit approximately the same amount of energy per unit length, no matter what the actual energies the depositing particle happens to have. This is an excellent opportunity to examine the prototype under circumstances similar to the actual experiment. The experimental techniques for cosmic ray runs are more involved than those for the radioactive source or LED testing. The luxury of the latter two is that they are both localizable, that is, they are able to be affixed to the detector wherever the testing dictates. The problem is that we wish to examine the response of the detector when cosmic rays passes through both scintillator arcs

and also when the cosmic ray is traveling roughly perpendicular to the face of the scintillators. The scattered electrons in the real experiment will traverse the detectors in this fashion. To accomplish this goal, the construction and use of two "trigger" counters were necessary.
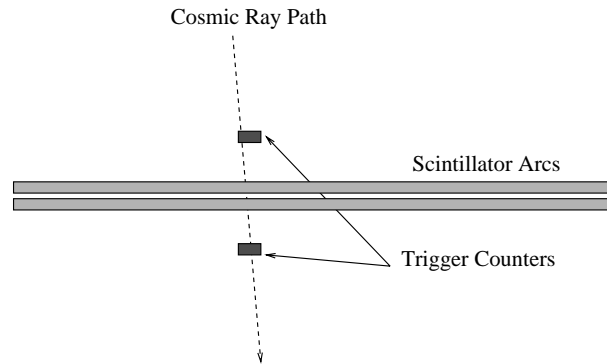
Figure 4.12: Setup for cosmic ray Studies

Both trigger counters were constructed using 3 cm Russian "FEU" PMTs, each with a 6.45 cm^2 square piece of 1 cm thick scintillator plastic affixed face down to the window of the PMT. As Fig. 4.12 shows, one of the trigger counters was placed above (T1) and one below (T3). The distance between the trigger counters and scintillators was approximately 3 cm. The small size of T1 and T3 and their close proximity to the detector scintillators creates a very clean setup that all but guarantees that if a cosmic passes through T1 and T3, it will definitely pass through the two detector scintillator arcs. With this setup, the efficiency of the G^0 prototype was easily determined.

The setup as it was ultimately configured is shown in Fig. 4.12. Initially, identical top and bottom trigger counters were not used. The top trigger

counter was a longer, rectangular counter. With this setup, the possibility of a geometric inefficiency could not be ruled out, thus prompting assembly of the second smaller counter. A geometric inefficiency would occur if a cosmic ray could pass through the larger top counter, miss the detector and go through the bottom counter. In this situation, the electronics would be tricked into thinking that a real cosmic went through the detector. This would give the detector a false inefficiency since any of these misses would have nothing to do with the detector itself. Figure 4.13 shows this case.
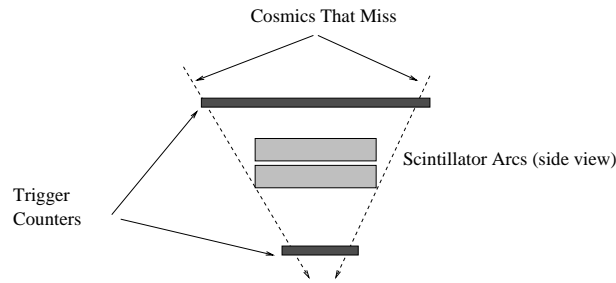
Figure 4.13: Cosmic ray setup with geometric inefficiencies (cross-section).

The DAQ electronics were set to trigger when a coincidence occurs between the top trigger, T3, and the bottom trigger, T1. This will occur when a cosmic ray provides a signal to T3 and T1, and the signals arrive at the discriminator module over threshold. To determine the efficiency of the detector during these cosmic ray studies, the TDC information of the various tubes were analyzed. The TDC measures the amount of time between the START, in this case, a signal in both T3 and T1 over threshold, and the STOP, the signal from each G^0 tube. The difference between the two arrival times of these signals

is entered in the TDC histograms and thus show the amount of time for a signal, going through the region of the detector defined by T1 and T3, to reach the electronics. Ideally this would be a spike, but since T1 and T3 defined a certain solid angle and have finite timing resolution, the TDC histograms show a peak with a non-zero width. The information within the histograms can help to determine the efficiency of the detector. The inefficiency is reflected in the form of overflows, which indicates that the trigger counters started the TDC but the signal from the tube(s) never arrived in the allotted time to stop the TDC. The signal was simply not seen by the detector. The number of overflows in each tube's TDC histogram divided by the total number of events that sent a start to the TDC is a measure of the inefficiency of the detector. The results of such a study is shown in Table 4.2.

PMT	number of real events	number of overflow events	Efficiency (%)
FL	2037 $\pm$45	63 $\pm$8	96.9 $\pm$0.05
FR	2035 $\pm$45	64 $\pm$8	96.8 $\pm$0.05
BL	2036 $\pm$45	63 $\pm$8	96.9 $\pm$0.05
BR	2033 $\pm$45	66 $\pm$8	96.7 $\pm$0.05

Table 4.2: Inefficiency for the four prototype PMTs. Voltages were set equal to values on Table 4.1. The discriminator threshold was set to 15mV. To gather $\sim$2000 events took multiple runs totaling more than 2 days total running time.

These results, although from relatively few events, indicate an efficiency of 97%. It is worth noting that all four tubes missed roughly the same number of events and that the overflow events in one tube are the same overflow events in the other three tubes, pointing to inefficiency in the trigger counters and not necessarily the G^0 detectors. Also, the data in Table 4.2 was obtained

without examining the pulse-height data from the T1 and T3 trigger counters. Placing cuts on these histograms, around the minimum ionizing peaks, would select out events where both T1 and T3 saw a minimum ionizing particle. Figure 4.14 shows a bidimensional plot of the ADC spectra of T1 vs. T3. The dark region in the middle of the plot corresponds to events where both trigger counters fired with a minimum ionizing pulse-height.
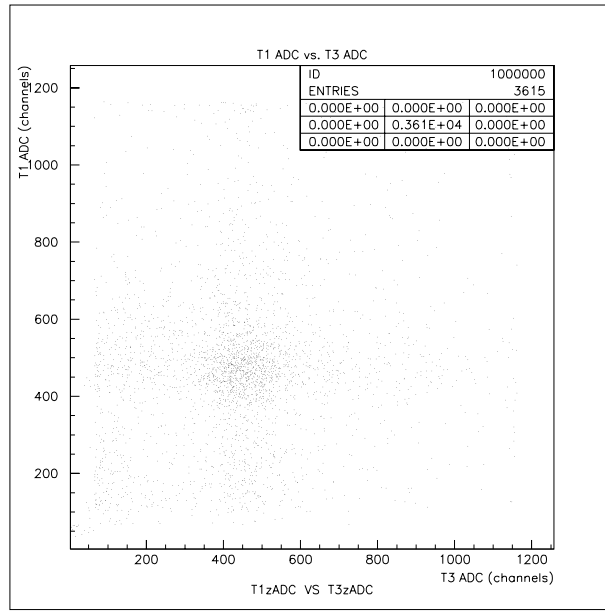
Figure 4.14: T1 ADC vs. T3 ADC. Notice the dark region in the middle where true minimum-ionizing cosmic-ray coincidences are clustered.

Recalculating the data in Table 4.2 with restrictive cuts on the trigger counters' ADC spectrum yields better results, although with reduced statistics. The confidence in these results could be undermined is there was a high probability of accidental coincidences between the two trigger counters. With noise rates of approximately 100 events per second and an ADC gate width of

100 ns, the probability of accidental coincidences is on the order of a part in a thousand.

PMT	number of real events	number of overflow events	Efficiency (%)
FL	734 ±27	1 ±1	99.9 ±0.1
FR	734 ±27	1 ±1	99.9 ±0.1
BL	735 ±27	0	100.0 ±0.1
BR	735 ±27	0	100.0 ±0.1

Table 4.3: Revised inefficiency for the four prototype PMTs. Restrictive cuts were placed on T1 ADC and T3 ADC (400 channels $\leq$ T1 ADC $\leq$ 600 and $375 \leq$ T3 ADC ≤ 600). Conditions are otherwise the same as is Table 4.2.

The results in Table 4.3 show that the G^0 prototype is nearly 100% efficient (this means that if a minimum ionizing particle passes through the scintillator arcs, it will be seen above the 15mV discriminator threshold and will be seen by the electronics and processed). In the actual experiment, successfully detected electrons or protons will be recorded through the use of a digital counter or "scaler". The experiment will not actually record individual scattered-particle events. This process is time consuming (due to the high data rate during the actual experiment) and ultimately unnecessary. Instead of backtracking to the number of incident electrons from the number of photoelectron's, the electronics of the actual experiment will be configured with a threshold sufficient to cut out noise and let real events through. When an incident particle is above this threshold, the scaler will be advanced. Since E91-017 expects to measure asymmetries on the order of 10^{-6}, inefficiencies can cause two significant problems. The first is that an overall reduced efficiency will increase the running time and will also decrease the statistical precision due to fewer events. Sec-

ond, any location-specific inefficiencies, like flaws in a particular region of the detector arcs, can lead to false asymmetries if, for example, the beam position changes when the electron beam is flipped from one helicity to another.

The data from cosmic ray runs can be used in conjunction with the single p.e. calibrations (Table 4.1) to determine how many photoelectrons are created by a minimum-ionizing particle traversing the detector. Each of the four ADC peaks from the main G^0 phototubes were divided by their appropriate "channels/p.e." calibration to yield the average number of photoelectrons for a minimum-ionizing cosmic ray. Results are shown in Table 4.4. An example of a typical cosmic ray ADC spectrum is shown in Fig. 4.15.
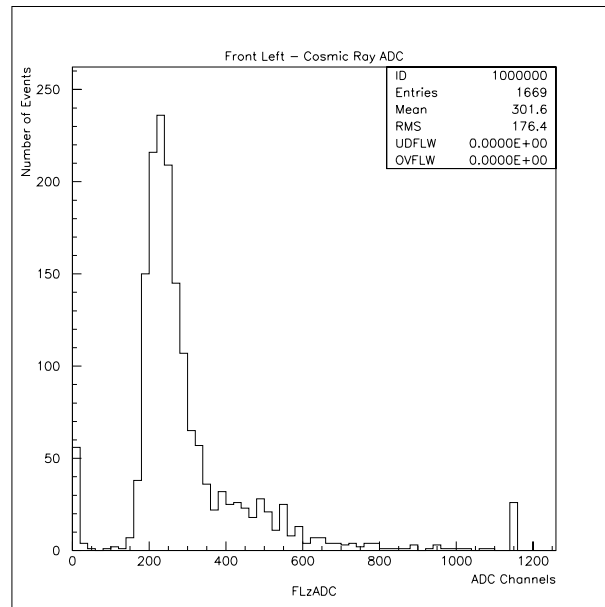

Figure 4.15: Typical cosmic ray ADC spectrum for the FL tube.

The next level of analysis is to determine the probability of losing p.e.'s

39

PMT	Channels/P.E.	Peak - ADC channels	Peak - p.e.'s
FL	1.77	227	128.2
FR	1.47	270	183.7
BL	1.82	256	140.7
BR	1.94	298	153.6

Table 4.4: ADC centroids for 4 G^0 PMTs scaled from channels to p.e.'s. These ADC centroid were collected at 15longitudinal source scan, Fig. 4.7. The number of p.e.'s correspond to a minimum-ionizing particle depositing approximately 2 MeV of energy in the 1 cm thick scintillators.

underneath the discriminator threshold. Even though signals from the PMTs come into the electronics well above threshold, there is a finite probability that, given an average number of photoelectrons per event, you will see a much lower number of photoelectrons for some events. Determining these probabilities will give another measure of efficiency for the detector in that, if the number of photoelectrons seen by the PMTs is too low, the discriminator threshold may start to cut into real events. To examine this characteristic of the prototype, first the number of photoelectrons per mV need to be determined. To do this, the DAQ was set to trigger on an OR between the FL and FR tubes. The ^{106}Ru source was placed on the front detector in the middle of the scintillator, both longitudinally and radially. After taking data, the FL ADC histogram was examined to see where the discriminator is cutting off the signal. The threshold was raised by 10 mV increments until there were enough "channel vs. threshold" points to plot. The result of this test, scaled from "channel vs. threshold" to "photoelectrons vs. threshold", is shown in Fig. 4.16. Note that the 15 mV threshold used in most of the present tests corresponds to
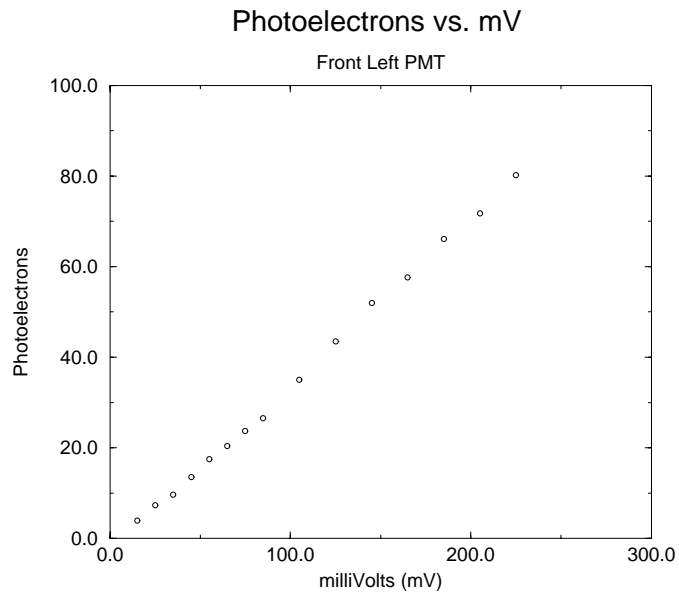
approximately 5 photoelectrons.

Figure 4.16: The number of photoelectrons per discriminator level (mV) for the FL tube. The ^{106}Ru source was used to collect these data.

To determine if a certain level of photoelectrons is dangerously low, i.e. events are lost due to the discriminator, the Poisson distribution function can be used. The Poisson distribution is given by

$$P(n; \mu) = \frac{\mu^n e^{-\mu}}{n!} \tag{4.1}$$

P(n;μ) is the probability that n photoelectrons will be seen when their mean is μ. Consider 80 photoelectrons (about 10 p.e.'s lower than the lowest p.e. level from Fig. 4.6) as our worst-case scenario. Also consider a discriminator set to 40mV or 10 p.e.'s (chosen to be well above the single p.e. level). To

determine how many p.e.'s will be missed, the distribution given in Eq. 4.1
needs to be summed over n, with n going from 0 to 10:

$$P(10; 80) = P(0) + P(1) + P(2) + ... + P(9) = 7.5 \cdot 10^{-22}\% \qquad (4.2)$$

This demonstrates that even with a worst case for μ and for a moderately
high threshold of 40mV, the number of photoelectrons missed by the tubes
is essentially zero. Even for a very large threshold of 100mV, the probability
that the phototube will miss photoelectrons due to the discriminator is 3.5
x $10^{-8}\%$. This is an encouraging result and it assures that with the number
of photoelectrons in table 4.4 (and even for a number much lower), the G^0
detector will see every scattered electron that hits the scintillators.

4.3   Timing Resolution

4.3.1   Importance of Timing Resolution

Another critical characteristic of the G^0 detector prototype that requires test-
ing is the timing resolution of the four phototubes. As described previously,
the two trigger counters define a small area of the scintillators for cosmic rays
to be detected and processed by the electronics. In an ideal situation, the
amount of time for signals to propagate from the designated area should be
constant, with the only variation being the path lengths of the photons. The
way to gauge the timing resolution of the detector is to examine the TDC
peaks of the various tubes, specifically the width of the peak. A wide peak
would signify that for the tight geometry defined by the trigger counters, the

time for signals to reach the TDC module is varying significantly. This could be caused by time jitter in the trigger counters. Jitter arises from the smaller trigger counter PMTs being electronically unstable and their timing fluctuating slightly during measurements. Jitter or fluctuation in the trigger counters will reflect equally in the TDC spectrum of all four G^0 PMTs since the two trigger counters set the timing.

An example of a TDC peak is given in Fig. 4.17. There is a tail on the left side of the peak. This is due in part to the size of the incoming signal and also to the behavior of the discriminator module. A larger pulse will hit the discriminator threshold earlier than would a smaller pulse due to an earlier rise time. This is known as "timing walk". Thus, the TDC stopped earlier for a larger peak.

4.3.2 Determining Timing Resolution

If a Gaussian function is fit to the peak, the sigma of the peak is a measure of the timing resolution. The sigma of the TDC peak is measured in channels and the conversion to real time is 59 ps / channel in the TDC histograms. For example, a timing peak with a sigma of 6 channels would translate to 354 ps. This would be a very encouraging number because it means that for real, meaningful events, all the signals from this particular tube will arrive at the electronics at a certain time (defined by the arbitrary length of the signal cables) ± 177 ps. The raw TDC histograms will not give widths this small without putting cuts on other related histograms. For example, looking at the FL TDC with a window around the ADC peak will give a narrower TDC
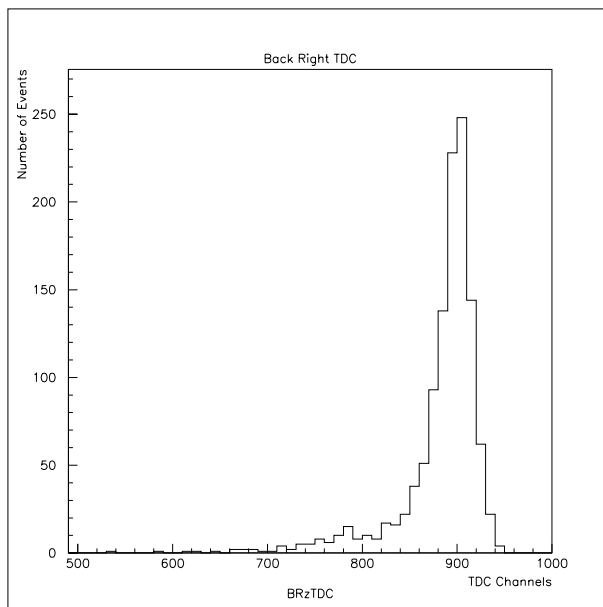
Figure 4.17: This histogram is the TDC peak for the BR Tube. Notice the tail on the left side. This could signify large peaks stopping the TDC early.

peak. Unfortunately, the trigger width is a little more difficult to suppress because it originates in the two trigger counters, where the timing for all four tubes is set. One way to suppress the trigger width is to subtract one tube's TDC peak from another's. Because the trigger timing effects both tubes' TDC peaks, performing this difference will subtract out the trigger width and leave a narrower peak. The resulting peak's position has no real meaning anymore, however, it is the width that is the important quantity. The width of the difference-peak (σ_D) is then given by the intrinsic timing (in the absence of the trigger's influence) widths of the two PMTs added in quadrature:

$$\sigma_D = \sqrt{\sigma_1^2 + \sigma_2^2}. \tag{4.3}$$

44

Assuming that σ_1 and σ_2 are equal, Eq. 4.3 can be reduced to:

$$\sigma_D = \sqrt{2}\sigma_i. \tag{4.4}$$

where σ_i is the intrinsic timing width of either tube. Thus σ_i is equal to

$$\sigma_i = \frac{\sigma_D}{\sqrt{2}}. \tag{4.5}$$

To calculate the width of the trigger timing, consider that the observed width of a particular PMT is the intrinsic width and the width of the trigger added in quadrature:

$$\sigma_{FL} = \sqrt{\sigma_i^2 + \sigma_{trigger}^2} \tag{4.6}$$

Solving for the width of the trigger is trivial. However, the jitter in the trigger counters is only present for the prototype. When E91-017 goes online, there will be no trigger counters and the experiment will only be subject to the timing resolution of individual G^0 detectors. According to the Cost and Design Report for the G^0 experiment, the timing resolution needs to be at or below 1 nanosecond [7]. The 1 ns limit was set for two main reasons. The first was to eliminate backgrounds such as non-elastic scattering events, "room-background", and cosmic rays. The second reason is that for certain detectors, the determination of Q^2 requires a cut on the timing because there can be two different particle paths (with different Q^2) that will arrive at the same detector.

Table 4.5 shows the timing using the cuts put on the T1 and T3 ADC histograms discussed in section 4.2.2. Using Eq. 4.6 and Table. 4.5, the
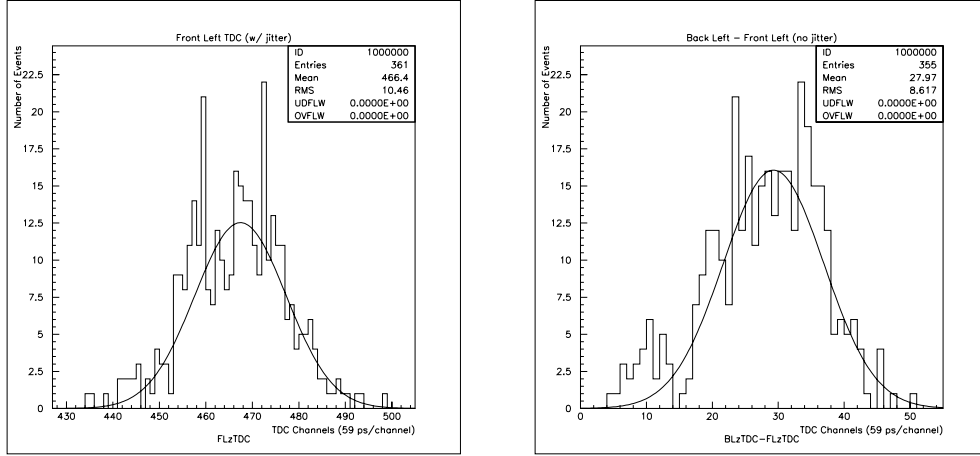
Figure 4.18: The left figure shows FL's TDC peak with trigger width added (σ: 578.2$\pm$29.5 ps). The right figure shows the TDC peak for BR - FL, where the trigger width has been removed (σ: 448.4$\pm$23.6 ps).

PMT	TDC peak width (channels)	TDC peak width (ps.)
FL	9.7	576
FR	11.0	652
BL	13.9	823
BR	10.1	599

Table 4.5: Timing resolution (σ) for G^0 prototype PMTs (with trigger counters). Note that using Eq. 4.6, the intrinsic widths are actually lower (see Eq. 4.5).

intrinsic width for FL PMT is approximately 320 ps (much better than 578 ps specified in Table 4.5) and the trigger width is approximately 480 ps. Even without performing the previous calculations, the values in Table 4.5 are in accordance with the 1 ns requirement set in the "Cost and Design Report" [7].

Chapter 5

Conclusions

The difficulty in assembling the detector prototype suggested that a few features need to be reevaluated. The jig used to form the light guides should be designed to hold the light guides in the same locations as they will be held on the support ribs. This would prevent any relaxing in the plastic and would prevent the need to repeatedly shim the light guides to mate them to the scintillators. Perhaps using fewer outside contractors might reduce the chances of letting flaws propagate unnoticed.

The Philips X2262 phototubes chosen for this experiment performed well. After a fifteen minute warm-up, the tubes provided nearly constant gains. This is especially apparent when two separate, but identically configured, cosmic runs were compared. The ADC peaks and TDC peaks both appeared in the same position. When the single photoelectron calibrations were being measured, the tubes provided clear peaks for both the pedestals and the p.e. peak, despite the location of the campus radio station transmitter 100 yards away. While the proximity of the radio station does have the effect of widening the single p.e. and pedestal peaks, it did not prevent measurements of their

centroids. The tubes performed equally well for the source and cosmic studies.

From the source scans, both longitudinally and radially, the G^0 detector prototype was shown to have the capability to detect minimum ionizing particles. While there is noticeable attenuation along ϕ and in the radial direction, the signals arrive at the PMTs with enough amplitude that this attenuation has little effect on the prototype's ability to resolve minimum ionizing particles.

When the ADC and TDC channels are properly timed, the prototype yields clean cosmic ray data. Examination of the TDC histograms, specifically the number of overflows, the prototype exhibits a very high efficiency of approximately 99.9%. When the ADC histograms for the cosmic runs were converted to p.e.'s versus channels, the detector yielded a number of photoelectrons well over the limit of 40 photoelectrons specified by the G^0 Technical Design Review [7]. The number of photoelectrons seen by the PMTs did vary depending on where ionizing particles traversed the scintillators. During the source scans, p.e. levels as low as 100 and as high as 240 were observed.

The timing resolution for the detector was studied and also yielded good results. Despite the presence of jitter in the trigger counters, the timing peak widths for the four PMTs came in well below the specified upper limit of 1 nanosecond [7].

The tests completed for the G^0 prototype focal plane detector have shown that the current design is capable of doing what it was designed to do, that is to measure asymmetries necessary to calculate the $G^0_{E,M}$ flavor-singlet charge form factors. The mechanical configuration might create some fabrication complications but these are minor considering the superb performance of the

detector as a whole. It is the opinion of the author that, barring the afore-mentioned mechanical hurdles, the construction of the full focal plane detector should commence with the knowledge that the detector prototype has passed every test asked of it.

Appendix A

Data Acquisition Electronics

A.1   TDC - Time to Digital Converter

The TDC module is responsible for recording the time difference between a Common Start (a start on a stopwatch for example) and a Stop. In the G^0 prototype, the Common Start is defined by the Coincidence unit. The Coincidence allows the experimenters to define the logical definition of an event.

In terms of the cosmic ray studies, a real event occurs when a cosmic ray traverses the two trigger counters with pulse heights over the discriminator threshold. Therefore, the Coincidence unit is set to T1·T3, which is a logical AND. The raw signals from T1 and T3 are sent to the Coincidence unit, where they both create a logic pulse. If these two logic pulses overlap, the coincidence condition is met and the TDC Common Start is set. The Common Start (AS) creates a pulse. When a signal from the four tubes and the two trigger counters reaches the TDC, a STOP pulse is created. The value incremented in the TDC histogram is the difference between each PMT's STOP and the CS. The TDC

histogram will show a peak corresponding to the mean arrival time of a cosmic ray signal, with a width corresponding to the intrinsic resolution of the PMTs, TDC module and the G^0 prototype itself. The widths of the PMTs correspond to the timing resolution of the prototype. The importance of this resolution is discussed in Section 4.3.

A.2   ADC - Analog to Digital Converter

The ADC module in the Data Acquisition electronics is responsible for the integration and digitization of an input voltage pulse, corresponding to a cosmic ray event. The GATE in the ADC module is assigned a specified width, and can be thought of as a flood gate. When the coincidence condition is met in the Coincidence unit, the GATE is opened, letting electric charge spill in for a specified width (time span). The amount of charge accumulated during the period which the gate is open is integrated and sent to an ADC histogram. Timing of the ADC GATE is important. If a signal from a PMT arrives before the gate has opened or after the gate has closed, a good physics event will be lost due to this poor timing. Also, if the signal arrives at the exact time the gate opens or closes, part of the pulse can be cut off and lost. It is best to calibrate the GATE timing with a radioactive source to ensure that the GATE will enclose the entire pulse.

The importance of a cosmic ray ADC histogram is that it displays the Gaussian distribution of the photon energies seen by the PMTs in the form of a peak. This peak can then be fit with a Gaussian and the value of the centroid is proportional to the energy deposited by the cosmic ray. The peak

centroid is given in ADC channels, which can be converted to photoelectrons. During the real experiment, ADC information will not be collected for every scattered particle due to a tremendous data rate. Occasionally, ADC and TDC information will be collected from the G^0 Focal Plane Detectors to make sure that the timing for each detector element is properly set. Real events must sacrificed during this period due to the fact that the rates at which the experiment will be running would be much too large for the ADC and TDC modules to handle. During the real experiment, the discriminator level will be high enough, to cut out noise, and low enough not to cut into relevant physics events. When a signal does arrive over threshold, it will be assumed that it is a scattered electron or proton, depending on the detector's configuration, and the scalers will be incremented.

A.3 Electronics Schematic

The following figure is a schematic of the electronics chain used during the testing of the G^0 prototype.
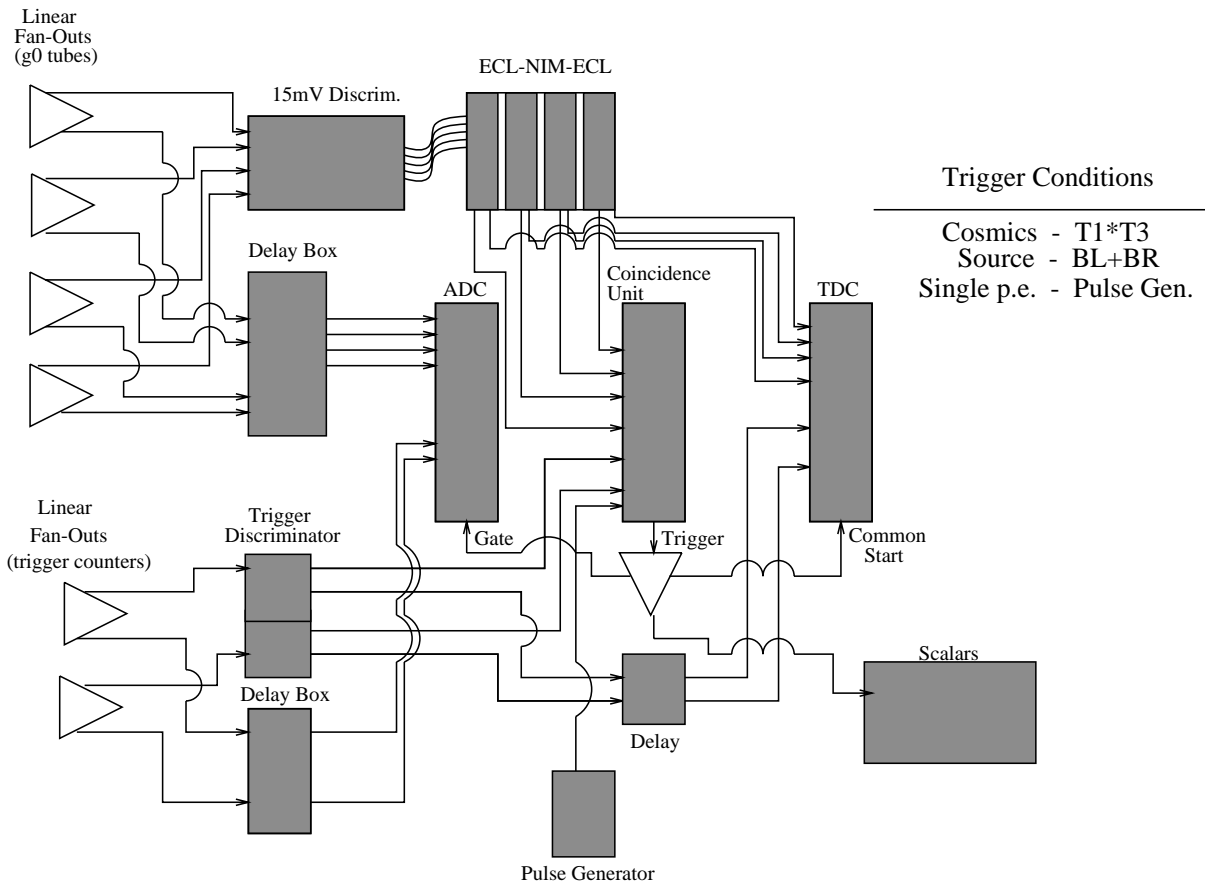
Electronics Schematic for Prototype DAQ

Trigger Conditions

Cosmics - T1*T3
Source - BL+BR
Single p.e. - Pulse Gen.

Figure A.1: Electronics Chain for the G^0 prototype DAQ. The trigger conditions are included for each configuration.

53

Bibliography

[1] L. Bergmann and C. Shaefer, *Constituents of Matter; Atoms, Molecules, Nuclei and Particles*, Walter de Gruyter & Co., New York, New York, USA, 1997.

[2] D. Beck, *CEBAF E91-017 proposal*, (1991) 2. (unpublished)

[3] R.D. McKeown , *Parity Violation in Electron Scattering*, (1997) 2. Contribution to Workshop on Parity Violation, held at L'Ecole Normale Superieur, Paris, France

[4] *Phys Rev. D; Particles and Fields*, **D50** (1994) 1251.

[5] E.H. Bellamy *et al*, *Nucl. Instrum. Meth.* **A339**, (1994) 468-476.

[6] *Appendix A to G^0 Technical Design Report*, (1997), 70. (unpublished)

[7] G^0 *Cost and Design Report Appendicies*, (1998), Detector section.